Violent collisions and multifragment final states in the $^{40}Ca + ^{40}Ca$ reaction at 35 MeV/nucleon

K. Hagel, M. Gonin,* R. Wada, J. B. Natowitz, F. Haddad, Y. Lou, M. Gui, D. Utley, B. Xiaó, and J. Li
Cyclotron Institute, Texas A & M University, College Station, Texas 77843

G. Nebbia, D. Fabris, G. Prete, and J. Ruiz
Istituto Nazionale di Fisica Nucleare-Legnaro, I-35020, Legnaro, Italy

D. Drain, B. Chambon, B. Cheynis, D. Guinet, X. C. Hu, A. Demeyer, and C. Pastor
Institut de Physique Nucléaire-Lyon, 69622 Villeurbanne Cedex, France

A. Giorni, A. Lleres, P. Stassi, and J. B. Viano
Institut des Sciences Nucléaires-Grenoble, 38026 Grenoble-Cedex, France

P. Gonthier
Hope College, Holland, Michigan 49423
(Received 10 May 1994)

The 4π multidetector AMPHORA has been used to measure yield distributions and energy spectra for products of the collisions in the reactions of ^{40}Ca with ^{40}Ca at 35 MeV/nucleon. Events of high multiplicity (≥ 10) for which $\geq 85\%$ of the total entrance channel atomic number is detected have been isolated and found to result from the most violent collisions which lead to excitation energies near 6 MeV/nucleon. A large fraction of these collisions lead to multifragment final states. A detailed comparison of the experimental data with results of various models indicates that statistical models which allow for expansion of the system or treat the multifragmentation process as a simultaneous disassembly are more successful than normal sequential binary models at reproducing the yield data and the event complexity inherent in the multifragment events. Quantum molecular dynamic (QMD) calculations are found to provide generally good agreement with the data but overestimate the proton and neutron emission. The agreement is significantly improved if an appropriate afterburner is used to deexcite the separated primary QMD fragments. The sensitivity of such hybrid calculations to the assumed matching time between the dynamical calculation and the afterburner has been explored. The experimentally filtered QMD calculations which provide good agreement with the experimental observables suggest that the most complex events observed in this work come not from the most central collisions, which decay more by light particle emission, but from a region of impact parameter $b/b_{max} = 0.5$. This suggests that angular momentum effects play an important role in the multifragment decay modes. A comparison of the present results with those for projectile fragmentation in intermediate impact parameter collisions of 600 MeV/nucleon ^{197}Au with Cu indicates that a similar multifragmenting system is produced in the two very different reaction systems.

PACS number(s): 25.70.Pq

I. INTRODUCTION

Accelerating heavy ions to intermediate energies between 20 and 100 MeV/nucleon provides the opportunity to produce nuclei at the limits of their stability in temperature and excitation energy. The recent literature contains a multitude of studies of the reaction products of violent heavy ion collisions [1–24]. Many of these studies focus on the characteristics of multifragment emission from highly excited nuclei resulting from central collisions [7], on time scales of multifragment emission [2,19,20], and on the excitation functions and asymmetries of multifragment decay of projectilelike fragments (PLF's) resulting from peripheral and midcentral collisions [21]. Other studies show evidence for an onset of volume emission of heavy fragments as the projectile energy is increased [22] and the disappearance of the production of heavy fragments with increasing projectile bombarding energy [11]. Extensive theoretical efforts to treat multifragment emission processes have also been underway for several years [13–16,18,23,24].

Nuclei heated to the limits of their stability may deexcite in a very complex fashion. Dynamical models predict that in the initial stages of the reaction, the composite system first undergoes significant compression and afterwards expands. The degree of this compression and expansion is governed by the equation of state (EOS). A combination of careful experimental and theoretical efforts in this area may provide the means of defining the nuclear equation of state.

For near-symmetric light mass systems various experiments and theoretical calculations [6,15] indicate that

*Present address: Brookhaven National Laboratory, Upton, NY 11973.

multifragmentation can be expected to become a significant process at laboratory projectile energies near 35 MeV/nucleon. In order to explore such a system, we have used a 4π detector to make measurements of the charged reaction products in the ^{40}Ca + ^{40}Ca reaction at 35 MeV/nucleon. We have then made comparisons of the data to the predictions of various models in an effort to more fully understand the reaction mechanism for the most violent collisions. To complement the 4π charged particle data, we have also measured neutron multiplicities in the ^{40}Ar + ^{40}Ca system using a neutron ball.

The experimental method and analysis are described in the next section. The different models employed in this study are introduced in Sec. III and the characterization of the system is described in Sec. IV. In Sec. V we show the comparisons of the data to the various models. In Secs. VI and VII we discuss some of the implications of our results. Our conclusions are presented in Sec. VIII. A Letter describing some earlier analyses has previously been published [25].

II. EXPERIMENTAL PROCEDURE

In the experiment 35 MeV/nucleon ^{40}Ca ions were incident on a ^{40}Ca target in the AMPHORA [26] detector at SARA (Système Accélérateur Rhône Alpes, Grenoble, France) as shown in Fig. 1. This detector consisted of 120 CsI phoswich detectors covering 82% of 4π, 92 of which were at angles less than 45°, and also included fast plastic detectors in front of the CsI detector. In order to select the most violent collisions, a multiplicity threshold requiring signals in 14 detectors was used in our on-line trigger. Most of the data presented in this paper result from runs with that high multiplicity threshold, but several separate runs were also performed with a trigger multiplicity threshold of 4. Hydrogen and helium isotopes were identified using pulse shape discrimination. Heavier elements were identified with approximately unit Z resolution up to Z=20, using the ultrafast light component from the plastic signal and the slow light component of the CsI signal. The energy calibration for protons was determined from the sharp cutoff in the energy spectrum which reflects the punchthrough energy.

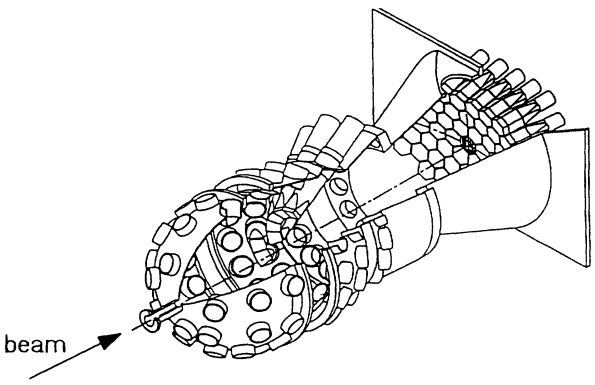

FIG. 1. The experimental configuration of the AMPHORA detector.

In a separate experiment, an ^{40}Ar beam from the Texas A&M K500 cyclotron was used at the same bombarding energy with a ^{40}Ca target in order to measure the neutron multiplicities in a 4π neutron ball [27]. The fast neutron ball signal was the trigger in this experiment and two detector telescopes were used to detect protons and α particles at the same angles as the detectors in AMPHORA. The telescope which was used at angles less than 90° consisted of three silicon detectors having thicknesses of 50, 400, and 2000 μm, respectively, backed by a CsI detector. The telescope which was used at angles larger than 90° consisted of four silicon detectors having thicknesses of 20, 260, 2000, and 5000 μm, respectively. A forward hodoscope consisting of a seven-strip 300 μm silicon detector backed by a 5 mm CsI detector was also employed to measure fragments between 3° and 8°. Data from these runs were used to verify energy calibrations for light particles in the AMPHORA experiment. The neutron ball experiments also provided neutron multiplicities and an independent confirmation of several important elements of the analyses of the AMPHORA detector as will be seen.

Energy calibrations for intermediate mass fragments (IMF's) in AMPHORA were determined by using the approximate beam velocity peaks in the forward angle spectra, observed during a singles calibration run, and determining quenching factors relative to the proton energies. The quenching factors deduced from the forward angle spectra were used for all of the detectors. The calibrations for angles of 4° and 6° were checked by comparing the energy spectra to those at corresponding angles in the ^{40}Ar + ^{40}Ca experiment, thus verifying the procedure. Uncertainties in the fragment energies are estimated to be ±10%.

III. MODELS

We describe in this section the models which we have used to compare with our data in our attempt to understand the reaction mechanism. The models used can be separated into three different categories. The first category consisted of the models that handle entrance channel dynamics only. These were important in this study because the symmetric system of ^{40}Ca + ^{40}Ca has a center of mass velocity equal to the nucleon-nucleon center of mass. This makes a separation of preequilibrium and equilibrium emission for the purposes of estimating the initial mass and excitation energy of the decaying system difficult. Included in our modeling of the entrance channel dynamics were a Vlasoz-Uehling-Uhlenbeck (VUU) model [14], a Boltzmann-Uehling-Uhlenbeck (BUU) model [28], the quantum molecular dynamics (QMD) models of Refs. [18] and [29], and a preequilibrium model [30].

The second category of models was composed of statistical models which follow the deexcitation of the excited nuclei. Included in these models were GEMINI [24], a sequential evaporation model which takes into account all

binary decay channels using the transition state formalism of Moretto [23], the simultaneous multifragmentation model of Gross [13], which assumes the simultaneous breakup of an expanded starting nucleus with $R_0 = 2.08$ fm and the expanding emitting source (EES) model of Friedman in which the sequential decay of an expanding nucleus is treated [16].

These first two categories of models were used together in order to model the collision in a hybrid fashion (analogous to that of Ref. [14]); that is, the entrance channel dynamical calculations were used to determine the initial conditions of mass, charge, and excitation energy of the deexciting system. The statistical model of interest was then activated in order to calculate the decay of the system.

The third category included the models which are intended to follow the entire evolution of the collision. These were EUGENE [31], an essentially phenomenological event generator based on massive transfer and preequilibrium assumptions and, on a more microscopic level, a QMD calculation [18] which starts with the entrance channel dynamics and follows the reaction to the final formation of clusters. This calculation, while similar in some respects to the BUU and VUU one-body models, provides a more realistic treatment of the fluctuations of the mean field and of cluster formation. In principle the QMD calculation should be able to simulate the entire reaction from the initial stages, where entrance channel dynamics are important, through the final deexcitation. In practice, however, we found that the QMD alone significantly underestimated IMF production and that better agreement with the data resulted from using the QMD model to describe only the first 100 fm/c of the reaction and then allowing the deexcitation of the excited fragments using GEMINI as an afterburner.

IV. CHARACTERIZATION OF THE SYSTEM

A. Selection of "complete" events

As indicated in Sec. II, an on-line multiplicity requirement of ≥ 14 detectors firing was used as the main trigger for data acquisition. Detection of electrons caused the firing of some detectors which were included in this multiplicity requirement. These detectors were excluded in the off-line analysis, which resulted in an effective charged particle multiplicity trigger near 10. Except where otherwise noted, data presented in this paper result from this high multiplicity trigger. This is done in an effort to emphasize the most violent collisions.

A combination of average velocity and multiplicity for all detected products has been used in several experiments [7,34,35] to select well characterized events. The average velocity is defined by the relation

$$v_{\rm ave} = \frac{\sum_{i=1}^{\nu} m_i v_i \cos\theta_i}{\sum_{i=1}^{\nu} m_i}. \quad (1)$$

In Fig. 2(a) we show the total multiplicity as a function of $v_{\rm ave}$ for the events taken with a multiplicity trigger of 4. For the lowest multiplicity events the average velocities are higher than $v_{\rm c.m.}$. With increasing multiplicity the distributions narrow and $v_{\rm ave}$ becomes $v_{\rm c.m.}$. In Fig. 2(b), we show the comparable distribution of average velocity for events with multiplicities in excess of 10. There the small spread in $v_{\rm ave}$ indicates very well characterized events.

In addition to demanding high multiplicity, we have also chosen to analyze only events in which at least 85% of the total atomic number Z of the combined system was detected. These analyzed events are virtually complete, missing only a few charged particles (most likely very forward preequilibrium protons). Since these "complete" events are only about 1% of the total number of recorded events, contamination by accidental events where two reactions occur within the same beam burst could be emphasized. To explore this possible contamination, we have constructed the spectrum of total energy shown in Fig. 3.

The total energy of an event was calculated by summing the kinetic energies of all detected particles together with the Q-value and appropriate corrections for neutrons. In this calculation, we estimated the neutron contribution by assuming the same number of neutrons as protons and neutron energies which differ from the proton energies only by the Coulomb energy. The solid histogram represents the experimental data for our analyzed events. We observe two peaks, one around 1100 MeV and the other around 1750 MeV. We attribute the first peak to the true events and the second to events in which two reactions occurred in the same beam burst. The low value of 1100 MeV compared to the 1400 MeV incident energy reflects the fact that for these events with $Z_{\rm tot} \geq 34$ the energy associated with six undetected protons and a corresponding six neutrons is missed in the summation. This is discussed further in Sec. V(b).

Using the results of the QMD calculation over the entire impact parameter range and filtered through the detector acceptance, we determine the $E_{\rm tot}$ spectrum which has a peak around 1300 MeV. That this is higher

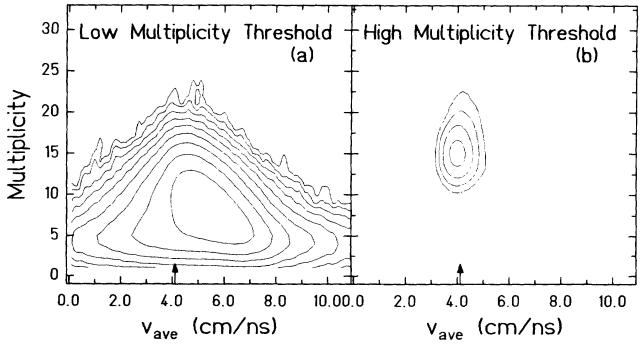

FIG. 2. Multiplicity vs average velocity of reaction products. The arrows indicate the center of mass velocity. (a) Low multiplicity threshold data and (b) high multiplicity threshold data.

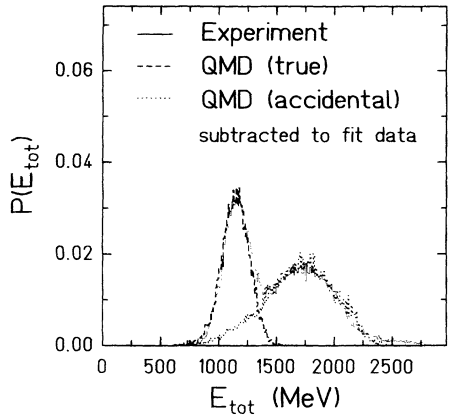

FIG. 3. The sum of the total energy of all reaction products. The solid curve represents the experimental data. The sharper peak around 1100 MeV results from the true reactions and the broader peak around 1750 MeV represents accidental events in which two reactions occurred in the same beam burst. The dashed curve represents the QMD calculation of total energy filtered through the detector acceptance and obtained in the same way as the experimental data. The dotted curve represents two events from the QMD calculation added together to simulate an accidental event.

than the 1100 MeV contained in the experiment suggests some difference between the results of the QMD calculation and the experimental data. We address this further in another section. If we simulate accidental events by adding together two random events generated by the QMD model and then filter those events through the detector acceptance, we obtain a distribution that has a peak near 1800 MeV. As these peaks do not match the data exactly due to the differences between the results of the QMD calculation and the experimental data, we have shifted them to fit the respective peaks in order to extract the accidental contribution. The results of the simulation after shifting the distributions by 200 MeV is shown for the true events as the dashed histogram in Fig. 3 and for the accidental events as the dotted histogram in Fig. 3. We see that the widths are reproduced quite well. Both of these peaks have been normalized to fit the data. We take the fraction of the accidental contribution in the true window as an estimate of our accidental rate. We estimate from this procedure an accidental rate of less than 10% after restricting the total detected energy of an event to be less than 1400 MeV as well as demanding that particles be in the true time peaks in the time spectra. Further tests show that contamination by random events does not affect the results sufficiently to change the conclusions of this paper.

B. Collision violence and centrality

Using the experimental data, it is possible to estimate the impact parameter range corresponding to the most violent events. We present in Fig. 4(a) the charged particle multiplicity distributions obtained from the experiment. The solid histogram shows the multiplicity distribution obtained from the low multiplicity trigger and the dotted histogram shows the multiplicity distribution resulting from the high multiplicity trigger. If we make the approximation that events with a multiplicity ≥ 4 represent the entire reaction cross section and that increasing

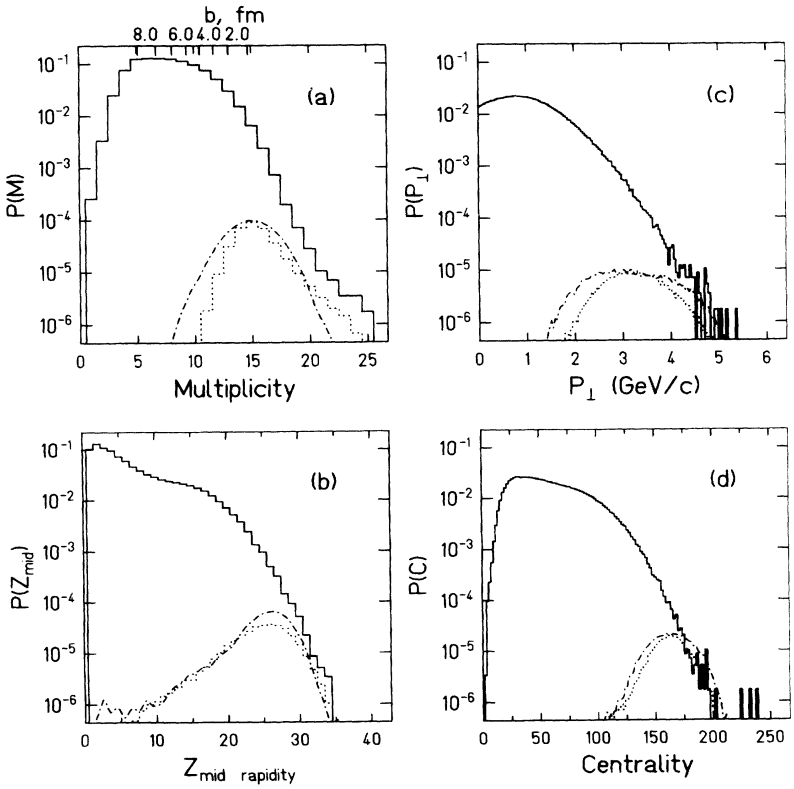

FIG. 4. (a) Experimental multiplicity distribution; (b) $Z_{\text{midrapidity}}$ distribution; (c) $p_\perp$ distribution; (d) centrality distribution, as described in the text. The solid curves represent the low multiplicity threshold data, the dotted curves represent the high multiplicity threshold data, and the dot-dashed curves represent the results of the QMD calculation after filtering through the detector acceptance. The impact parameter scale shown at the top of (a) indicates the impact parameters expected for corresponding multiplicities as discussed in the text.

multiplicity is associated with decreasing impact parameter, we can estimate the impact parameter using the following relationship:

$$b = b_{\max}\left\{\int_{M(b)}^{\infty} P(M)dM\right\}^{1/2}, \quad (2)$$

where $P(M)$ is the normalized multiplicity distribution. This procedure gives the impact parameter ranges shown at the top of Fig. 4(a). Comparing this impact parameter scale to the dotted histogram leads to an estimate that most of the "complete events" result from collisions having impact parameters less than 4 fm.

Other variables have been used in the literature in an attempt to determine impact parameters [6,32]. In Fig. 4(b) we show the distribution of midrapidity charge [32,33]. In Fig. 4(c) we show the distribution of the sum of perpendicular momentum. In Fig. 4(d) we show the distribution of centrality as defined by [6]

$$C = \left(\frac{M}{M_{\max}}\frac{p_{\perp}}{p_{\text{proj}}}\frac{Z_{\text{midrapidity}}}{Z_{\text{tot}}}\right)^{1/3}. \quad (3)$$

As in Fig. 4(a), the solid histograms represent the low multiplicity data and the dotted histograms represent the high multiplicity data with "complete events" selected. For each parameter represented in Figs. 4(a)–4(d) we observe that, to the extent a higher value of the selected parameter is associated with a lower impact parameter, our complete events result from the most central collisions. Using only the selection criterion of $Z_{\text{tot}} \geq 34$ on the low multiplicity threshold data isolates the same event regions as shown in Figs. 4(a)–4(d).

To estimate the fluctuations in our selection of the most central collisions, we have used reaction simulations. In Fig. 5 we present impact parameter distributions calculated with EUGENE [31] (open circles) and with the QMD model [18] (dot-dashed histogram) with no filter applied. The calculations have also been filtered through the acceptance of our detector, demanding a multiplicity ≥ 10 and $Z_{\text{tot}} \geq 34$. The resultant distributions are represented by the solid points for the EUGENE calculation and by the solid histogram for the QMD calculation. In these calculations, the events which pass the filter are from low impact parameters, mostly less than ≈ 4 fm, but the more microscopic QMD calculation implies some contribution up to 7 fm. For comparison with the experiment the parameter ranges in multiplicity, midrapidity Z, $p_{\perp}$, and "centrality" corresponding to the filtered QMD events are also presented as dot-dashed curves in Fig. 4.

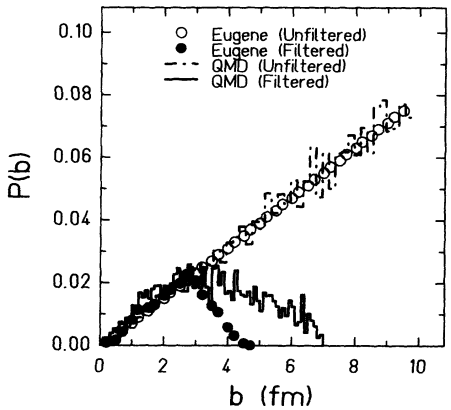

FIG. 5. Impact parameter distribution from model calculations. The open circles represent the unfiltered EUGENE calculation and the solid circles represent the EUGENE calculation filtered through the detector acceptance. The dot-dashed line and solid line represent, respectively, the unfiltered and filtered impact parameters predicted by the QMD calculation.

C. Primary composite system

To make comparisons of the data to results of statistical model calculations the mass (A) and excitation energy (E^*) of the deexciting system must be specified. For this symmetric system the experimental separation of preequilibrium and equilibrium emission from the particle spectra is difficult. Nevertheless, if we assume for the events selected that all preequilibrium products are emitted at very forward angles and escape through the beam pipe and that we are left with only products emitted from the equilibrated source, we can estimate the excitation energy by using the same procedure as was used in obtaining the results in Fig. 3, by excluding the energy of the center of mass. For our complete events the distributions of Z_{tot}, excitation energy, and A_{tot} (derived from Z by assuming the most probable isotope for a given detected atomic number) are shown in Fig. 6. We note a most probable value of $Z \approx 35$, a most probable value of $A \approx 75$, and a most probable value of E^* of 468 MeV.

We have also used several dynamical models to estimate the starting conditions of Z, A, E^* and angular momentum (J_{crit}) for the subsequent deexcitation calculations. Landau-Vlasov [14,15], BUU [28,36], and QMD [18,29] calculations indicate that at 35 MeV/nucleon the collision of ^{40}Ca + ^{40}Ca results in an initial compression followed by expansion. The system reaches maximum compression at about 70 fm/c. During this period significant preequilibrium emission occurs. Based on the calculations of Ref. [14], on BUU calculations using the codes of Refs. [36] and [28], on the QMD calculations of Refs. [18] and [29], and on preequilibrium emission estimates using the Boltzmann master equation [30] we have chosen A=70, Z=34, and E^*=420 MeV as the starting point for our deexcitation calculations. A maximum $J = 80\hbar$ is also indicated by the calculations. This is a slightly smaller system than calculated using the experimental data, but E^*/A remains approximately the same. In the QMD calculations that we performed using the model of Ref. [18], the quadrupole moment of the momentum distribution has a minimum near 0 at 100 fm/c. We therefore stopped the QMD calculation at that time and followed the deexcitation of excited products with the code GEMINI as an afterburner. We have chosen to be guided by the results of the dynamical models because we believe that in the experiment we do detect some preequilibrium particles at the more forward angles.

The observables that we calculate do not change appreciably for 20% variations of initial mass and excitation energy. Furthermore, in most of the models, excitation energies and mass transfers correlate in such a way as to maintain E^*/A relatively constant. Initially all model calculations are made assuming a single $A = 70$ source. In Sec. V C we discuss the effect of varying the time at which the QMD calculation is stopped and the afterburner is utilized. In Sec. VI we discuss the possibility of contributions from a more complex binary source.

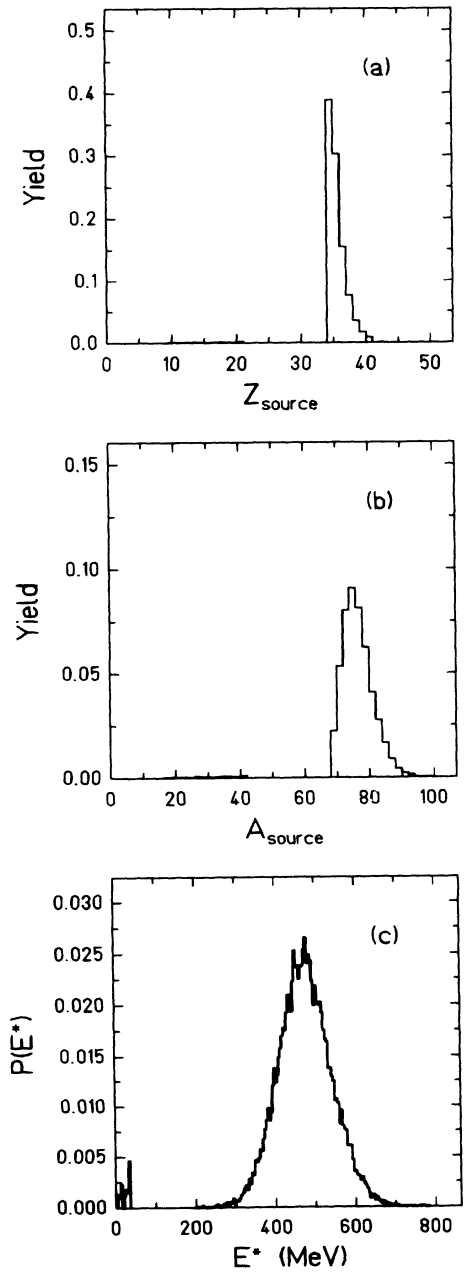

FIG. 6. Characteristics of the deexciting source extracted from experimental data assuming all preequilibrium products are missed. (a) The atomic number of the source, (b) the mass of the source, and (c) the excitation energy of the source.

V. EXPERIMENTAL OBSERVABLES

A. Light charged particle multiplicities

The solid points in Figs. 7(a)–7(e) represent the multiplicities and multiplicity distributions for the different species in our "complete" events. In the experimental data we find an average multiplicity per event of 6.1 protons, 5.4 α particles, and 2.4 intermediate mass fragments (IMF's, $Z \geq 3$). The models differ in their ability to reproduce these basic multiplicity observations (in comparing with the statistical model calculations we have added two protons to each event to simulate preequilibrium protons which were detected in the experiment). With this correction, the multifragmentation calculation of Gross [13] reproduces the proton multiplicity distribution very well, but predicts too few α particles and too many IMF's. The GEMINI [24] calculation, using $J_{crit} = 80\hbar$, predicts too many protons, and too few α particles. The QMD [18] calculation with the GEMINI afterburner overpredicts the number of protons by almost a factor of 2, predicts an average of only 1 α particle, and matches the IMF multiplicity distribution very well. The predictions of the proton and α-particle multiplicities by the QMD calculation might be improved by including antisymmetrization in the QMD. Indeed in an antisymmetrized molecular dynamics (AMD) [37] model a large increase in the calculated α-particle multiplicity is observed.

In Fig. 7(d) it is observed that only the Gross multifragmentation calculation comes close to reproducing the correlation of proton and IMF multiplicities while none of the calculations we have considered reproduce the correlation of α-particle and IMF multiplicities as seen in Fig. 7(e).

B. Neutron-charged particle correlations

Figure 8(a) shows the background corrected neutron multiplicity distribution obtained from our ^{40}Ar + ^{40}Ca experiment in the neutron ball. Figure 8(b) presents the measured average multiplicities of protons (open circles) and α particles (open squares) as a function of the detected neutron multiplicity. The proton and α-particle multiplicities initially increase with an increasing number of detected neutrons but become essentially constant above six detected neutrons.

In these experiments the neutron ball counting cycle was triggered by the fast light flash which signals the occurrence of a reaction. Since essentially all reactions lead to a sufficient number of γ rays and neutrons to produce this reaction trigger, the distribution of neutron multiplicities in Fig. 8 represents the total reaction cross section σ_R to a very good approximation. Association of the approximately 20% of the reactions which result from impact parameters ≤ 4 fm with the largest number of detected neutrons would suggest that collisions leading to ≥ 6 detected neutrons are the collisions analogous to those selected in the AMPHORA experiment. For such neutron multiplicities we note that both

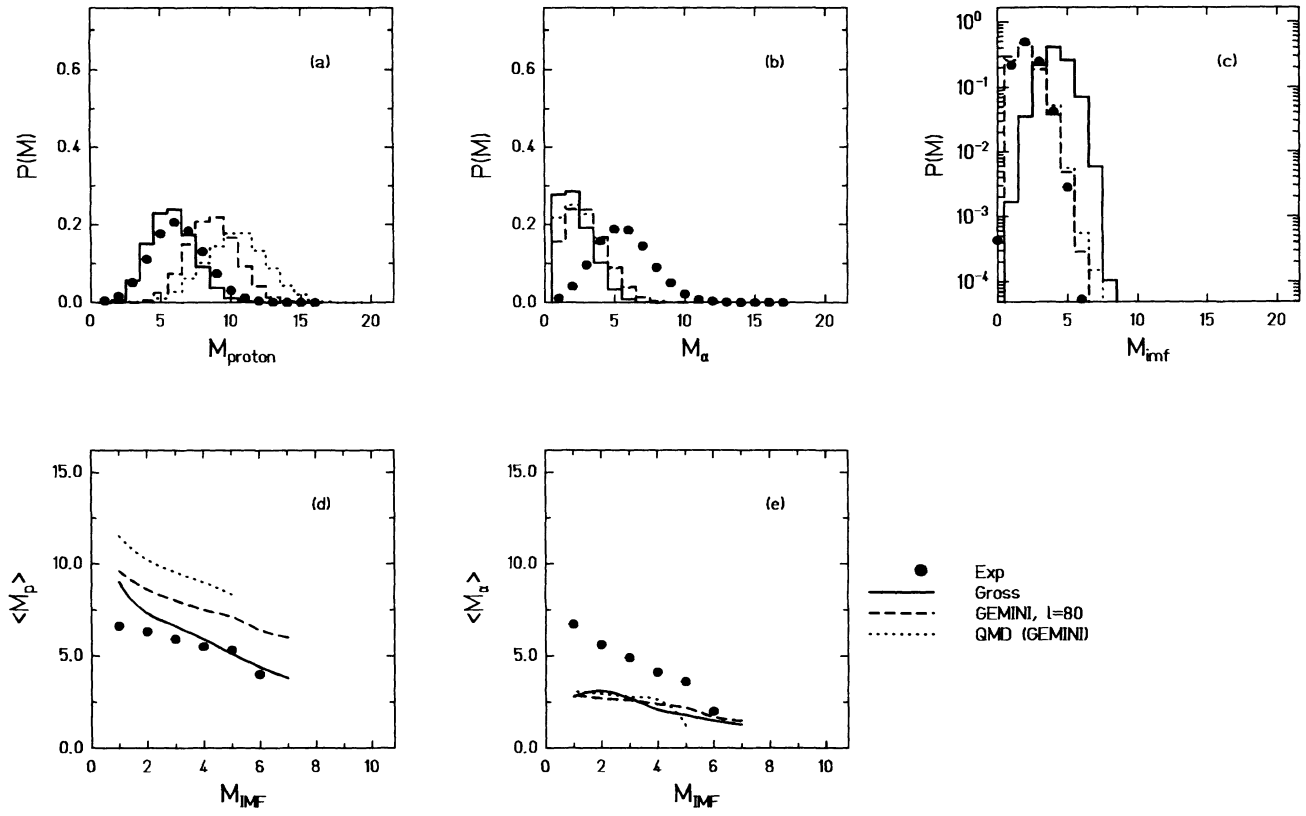

FIG. 7. Multiplicities of various products. The solid points represent the experimental data, the solid lines represent the predictions of the Gross multifragmentation calculation, the dashed lines represent the prediction of the GEMINI calculation, and the dotted lines represent the prediction of the QMD calculation with the GEMINI afterburner. (a) Proton multiplicity, (b) α particle multiplicity, (c) IMF multiplicity, (d) proton multiplicity vs IMF multiplicity, and (e) α particle vs IMF multiplicity.

the average α-particle and average proton multiplicities are essentially constant. This indicates that, for that region of detected neutron number, the distribution is dominated by the combined fluctuations in the neutron emission probability and detection. Indeed, a reconstruction of the primary neutron distribution, based on a simulation of the detector efficiency for this reaction [38–40], indicates that the average primary neutron multiplicity which leads to ≥ 6 detected neutrons is 11 ± 1. The value of $\langle M_\alpha \rangle = 5.2$ which is observed in this experiment confirms that measured for the central events in the AMPHORA experiment and underlines the utility of the neutron ball as a centrality filter, even for light systems. The value of $\langle M_p \rangle = 12$ is six protons more than that seen for $Z_{\rm tot} \geq 34$ events selected in the AMPHORA experiment. This reflects the fact that this multiplicity derived by integration of the measured angular distribution accounts for the entire proton emission into 4π sr and is not subject to the geometric losses in the AMPHORA detector. The observance of an average of 12 protons in these events confirms that the missing charge in the AMPHORA experiment is to be found in undetected protons.

Finally we note that in the reconstruction of the total energy for Fig. 3 it was assumed that the multiplicity of neutrons was essentially equal to that of the detected protons. This experiment confirms that expectation. However, we see now that both experimental multiplicities are significantly higher than those of the detected protons in AMPHORA. Proper accounting for these multiplicities allows reconstruction of the total 1400 MeV available in the entrance channel.

C. Elemental yield distributions

We present in Figs. 9 and 10 the experimental elemental yield distribution, as solid points, and the corresponding distributions predicted by different statistical models, as histograms, all filtered through the acceptance of the detector. The solid line represents the prediction of the simultaneous multifragmentation calculation of Gross [13] and the dotted line shows the prediction of the statistical code, GEMINI [24] with $J_{\rm crit}$ chosen to be $80\hbar$. For the experimental events, we note a steep falloff in yield between $Z = 1$ and 4, and then a more gradual decrease with increasing Z. The simultaneous multifragmentation calculation produces a charge distribution which falls off somewhat faster than the experimental distribution and produces more products in the range of $Z = 3$–10. Since the yield distribution is quite sensitive to excitation energy, reducing the assumed excitation energy improves

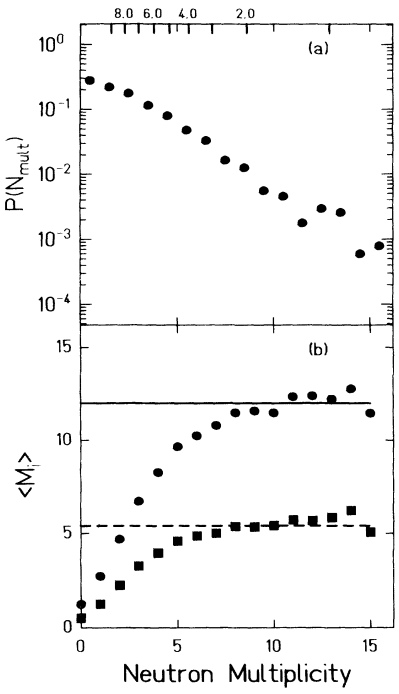

FIG. 8. (a) Neutron multiplicity distribution for the ^{40}Ar + ^{40}Ca system. (b) Proton (circles) and α-particle multiplicity vs neutron multiplicity. The horizontal solid line indicates the average proton multiplicity observed in the ^{40}Ca + ^{40}Ca experiment plus 6 to account for the missed preequilibrium protons and the horizontal dashed line indicates the average α-particle multiplicity observed in the ^{40}Ca + ^{40}Ca experiment.

the fit [12,13]. In Fig. 9 we also present the charge distribution predictions of this calculation at E^*=340 MeV. The calculation does provide a significantly improved fit to the entire data set although the yield is still overpredicted in the range of $3 < Z < 8$. Given our experimentally estimated excitation energy as well as those of the dynamic models, this reduction of the excitation energy to improve the fit to the yield distribution is probably not justified.

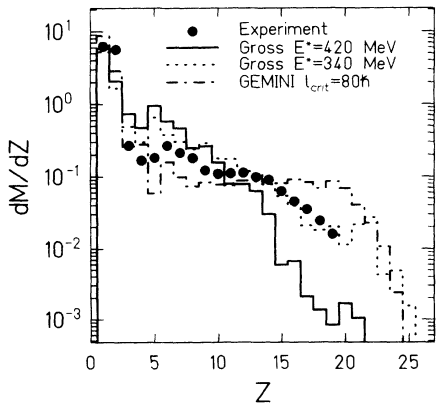

FIG. 9. The elemental charge distribution. Solid points represent the experimental data, the solid line represents the prediction of the Gross multifragmentation model for $E^* = 420$ MeV, the dotted line represents the prediction of the Gross multifragmentation model for $E^* = 340$ MeV, and the dot-dashed line represents the prediction of the GEMINI calculation.

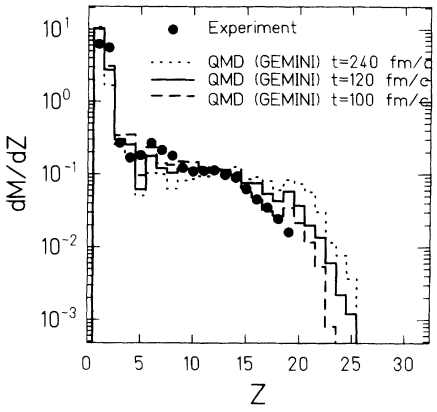

FIG. 10. The elemental charge distribution. The data (solid points) are compared with results from three different calculations in which the GEMINI afterburner is turned on at different times after the collision. These times are 80 fm/c (solid line), 100 fm/c (dotted line), and 240 fm/c (dashed line).

GEMINI produces the typical Z distribution expected from a normal statistical model, that is, a relatively large production of $Z = 1$ and 2 and a peak corresponding to heavy residues at higher Z. A lower excitation energy would lead to poorer agreement with the data.

Figure 10 presents a comparison between the experimental yield data and results of a QMD calculation with GEMINI afterburner for three different choices of the time at which the afterburner is activated. Using the relatively long time of 240 fm/c leads to a rather poor agreement with the experiment, characterized by too great a yield of high atomic number products and a deficiency of IMF's. Following the QMD calculation to longer times leads to only a small improvement because the subsequent decay in the QMD calculation is by light particle emission. As a result the excess of heavy products and deficiency of IMF's remains. In contrast, applying the afterburner at the earlier times of 100 and 80 fm/c significantly improves the fit since more complex fragments are emitted in that deexcitation calculation.

Although the best agreement with the yield distribution is obtained by turning on the GEMINI afterburner after 80 fm/c, the quadrupole moment calculation (see Sec. IV C) indicates that the system is not yet equilibrated at that point. In addition in intermediate impact parameter reactions which lead to two large fragments in the exit channel 80 fm/c is not enough time for the fragments to separate. We therefore choose to make comparisons of the QMD calculations to the data for the case when the GEMINI afterburner is activated after 100 fm/c. Due to the close proximity and therefore relatively large amounts of Coulomb energy of all QMD products at 100 fm/c, we integrated the Coulomb trajectories of all primary fragments and used the corrected velocities and directions as the input into the afterburner.

D. Event complexity

In Fig. 11 we show correlations between the fragment size and multiplicity. The figure shows the probabilities of detecting at least n fragments which have Z greater than or equal to a specified value which we call $Z_{\text{threshold}}$. The symbols represent the probabilities for n=1, 2, 3, 4, etc. For the data, shown in Fig. 11(a), we note that up to six fragments having $Z \geq 3$ are observed in some events. Figures 11(b), 11(c), and 11(d) show the predictions of the simultaneous multifragmentation model [13], the statistical model, GEMINI [24], and the QMD calculation [18] with the GEMINI afterburner, respectively. We note that the Gross model provides reasonable agreement with the data, but produces higher numbers of highfold events than seen in the experiment. The standard sequential model GEMINI, shows higher probabilities for emission of larger fragments and somewhat lower probabilities for multiple fragment emission than are seen in the data. The QMD (GEMINI) calculation shows very good overall agreement with the experimental data.

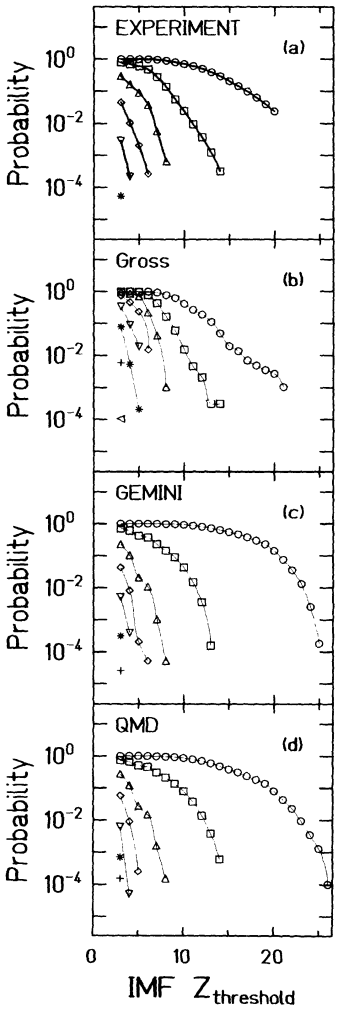

FIG. 11. Probability distributions for emission of at least n fragments, each having $Z \geq Z_{\text{thresh}}$. Symbols are $n = 1$, ○; $n = 2$, □; $n = 3$, △; $n = 4$, ◇; $n = 5$, ▽; $n = 6$, ∗; $n = 7$, +; $n = 8$, ◁.

As another means of exploring moments of the multiplicity distribution, we show in Fig. 12 the event-by-event distribution of the logarithm of the atomic number of the largest fragment of an event versus the logarithm of S_2', the normalized second moment of the event Z distribution, with the largest fragment excluded,

$$S_2' = \frac{\sum_{i:Z\neq Z_{\max}} Z_i^2 M(Z_i)}{\sum_{i:Z\neq Z_{\max}} Z_i M(Z_i)}. \tag{4}$$

Campi has suggested [41] the use of such a plot to search for possible critical behavior in deexcitation patterns.

Two peaks occur in the experimental contour plot in Fig. 12(a). One is located at large values of $\ln Z_{\max}$ and small values of $\ln S_2'$ and the other is located at small values of $\ln Z_{\max}$ and large values of $\ln S_2'$. The results of the multifragmentation calculation in Fig. 12(b) show only one peak at large $\ln S_2'$, similar to but at higher

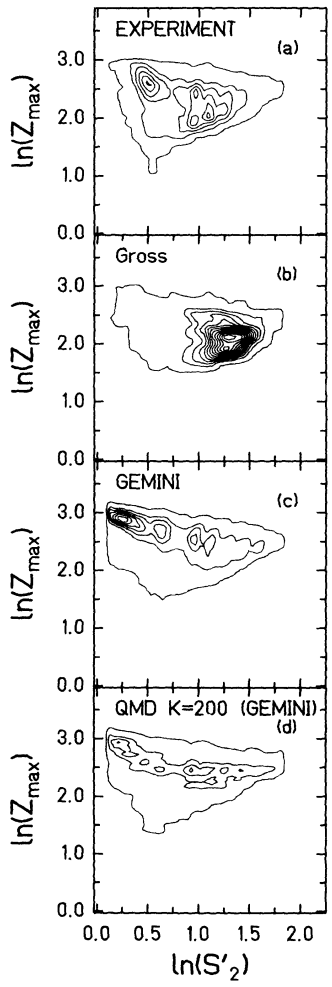

FIG. 12. Logarithmic distribution of $Z_{\max}$ vs S_2' (see text). Each contour represents constant value in units of relative $\frac{d^2Y}{d\ln S_2' d\ln Z_{\max}}$ where Y is the yield. The outside contour is at a level of 10, and each inner contour represents a progressive increase in yield of 150. (a) Experiment, (b) multifragmentation calculation of Gross, (c) GEMINI calculation, and (d) QMD model with GEMINI afterburner.

value than, the most prominent peak in Fig. 12(a). The GEMINI calculation, [Fig. 12(c)], on the other hand, produces a large peak only at small values of $\ln S_2'$, even lower than the lower peak in the experimental data, a fact which reflects the dominance of light particle emission in the GEMINI calculations. The QMD (GEMINI) calculation [Fig. 12(d)] predicts a spread of events over the entire $\ln S_2'$ range, more in line with the experimental data, but the peak at lower $\ln S_2'$ is at a lower value than that of the experimental data as, in the GEMINI calculation. In each case, QMD and GEMINI, this shift to a lower value reflects the fact that the proton multiplicities in the calculation are higher and the α multiplicities lower than in the experimental data.

Since the filtered simultaneous multifragmentation calculation is dominated by high $\ln S_2'$ events and the GEMINI calculation by low $\ln S_2'$ events, it is of interest to compare the yield distributions of these calculations with the respective yield distributions for high and low $\ln S_2'$ events in the experimental data. In Fig. 13(a) we compare the experimental charge distribution corresponding to the large $\ln S_2'$ peak with the prediction of the Gross multifragmentation calculation. We note a generally good agreement between the multifragmentation model and the charge distribution gated on large $\ln S_2'$ although the multifragmentation calculation again predicts some excess of products in the range of $Z = 3$–5. A comparison of these large $\ln S_2'$ events to the multifragmentation calculation at 340 MeV displays better agreement as shown by the dotted line in Fig. 13(a) but suffers from an overprediction at the largest charges. We compare in Fig. 13(b) the experimental charge distribution gated on small $\ln S_2'$ to the results of the GEMINI calculation. In this case we observe that although the curves are qualitatively similar, they do not agree very well. The peak of the GEMINI calculation extends to higher Z values than those observed in the experiment.

The dashed lines in Fig. 13 represent the prediction of the QMD calculation gated on small and large $\ln S_2'$ events, respectively. The agreement is seen to be quite good for large $\ln S_2'$ events over the full range of atomic number but suffers from the same overprediction of higher Z values as does GEMINI.

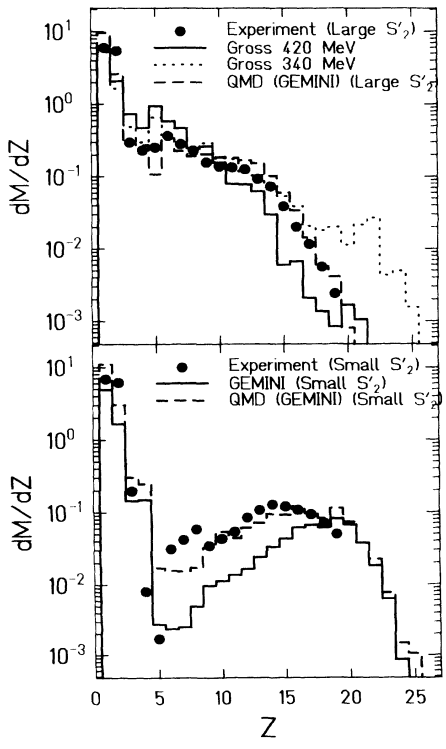

FIG. 13. The elemental charge distribution gated on small $\ln S_2'$ (top panel) and large $\ln S_2'$ (bottom panel). The dashed lines indicate the prediction of the QMD calculation gated on small and large $\ln S_2'$. The solid line in the top panel represents the prediction of the GEMINI calculation and the solid line in the bottom panel represents the prediction of the Gross multifragmentation calculation.

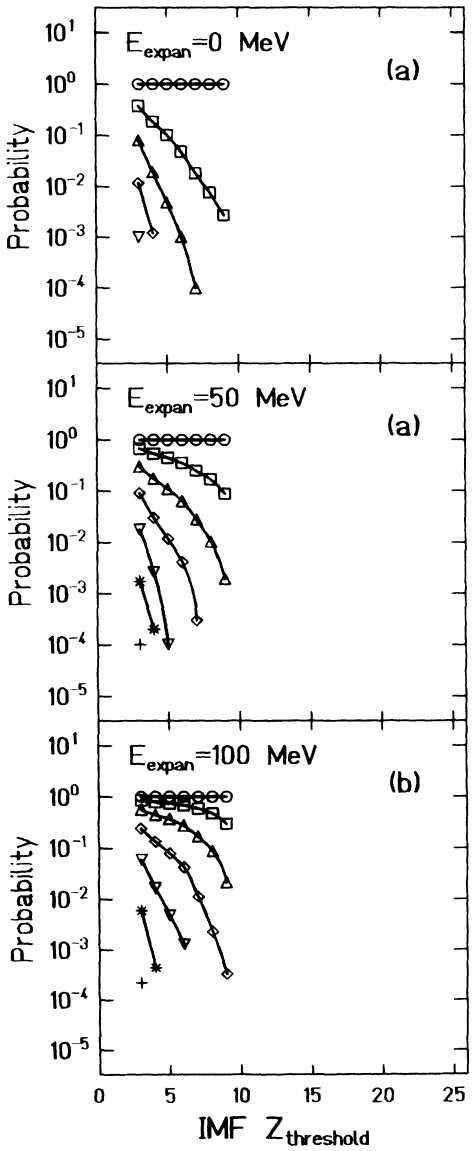

FIG. 14. Probability distributions for emission of at least n fragments, each having $Z \geq Z_{\text{thresh}}$ predicted by the EES model of Friedman. Symbols are $n = 1$, ○; $n = 2$, □; $n = 3$, △; $n = 4$, ◇; $n = 5$, ▽; $n = 6$, ∗; $n = 7$, +; $n = 8$, ◁.

The comparisons presented in Figs. 9, 11, 12, and 13 as well as those with results of the sequential evaporation code of Richert and Wagner [42] as presented in Ref. [25] suggest that "normal" statistical models are not in good agreement with the observations and that important dynamical effects must be taken into account. Since expansion of the nucleus is a key ingredient in the reasonably successful simultaneous multifragmentation model and is also important in the QMD model, a sequential statistical model which explicitly treats expansion effects may offer some particular insights to the multifragment emission process [43,44].

We present in Fig. 14 the correlations between fragment size and multiplicity obtained using the EES model of Friedman [16] and assigning an increasing fraction of the total excitation energy to an isotropic expansion of the system. The assumed expansion energies are indicated in the figure. This model limits IMF emission to $Z \leq 9$. The multiple fragment emission probability increases significantly with increasing expansion energy. A comparison to the data presented in Fig. 11(a) suggests that an assumed expansion energy ~50 MeV leads to reasonable agreement with the data.

In Fig. 15 we present plots of $\ln Z_{\max}$ vs $\ln S_2'$ for the different assumed values of E_{expan} of the deexciting system. As shown in Fig. 15(a), when $E_{\text{expan}} = 0$ the results are qualitatively similar to the GEMINI prediction. However, for $E_{\text{expan}} = 50$ or 100 MeV, as shown in Figs. 15(b) and 15(c), respectively, the distributions evolve to include events with larger values of $\ln S_2'$ and smaller values of $\ln Z_{\max}$. For $E_{\text{expan}} = 100$ MeV, the results shown in Fig. 15(c) are similar to those of the multifragmentation model which are presented in Fig. 12(b). Comparing the results of the calculations presented in Figs. 14 and 15 with the corresponding experimental results shows that the data could be reasonably well reproduced by the EES model with an expansion energy of 50–75 MeV or 0.75–1.0 MeV/nucleon. Again the need to incorporate some dynamics is indicated by this result.

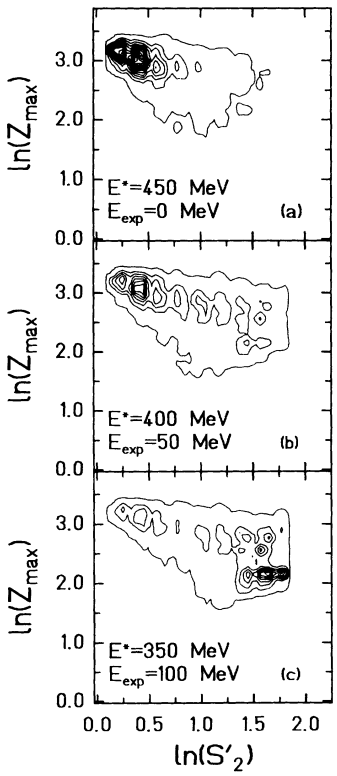

FIG. 15. Logarithmic distribution of $Z_{\max}$ vs S_2' (see text). Each contour represents constant value in units of relative $\frac{d^2Y}{d\ln S_2' d\ln Z_{\max}}$ where Y is the yield for the EES model of Friedman having E_{expan} of (a) 0 MeV, (b) 50 MeV, and (c) 100 MeV. The outside contour is at a level of 10, and each inner contour represents a progressive increase in yield of 150.

E. Energy spectra and angular distributions

Comparisons of experimental and calculated energy spectra and angular distributions of emitted particles and fragments may provide some further insights into the question of expansion. Figure 16 shows energy spectra of protons for the different angles in the AMPHORA detector compared to the results of the multifragmentation calculation, the GEMINI calculation, and the QMD (GEMINI) calculation, respectively. The multifragmentation calculation predicts proton spectra which peak at energies well below the energies observed in the experiment. This is a direct consequence of the lower barriers which result from the expanded nucleus in this calculation. Proton spectra predicted by the GEMINI calculation peak at energies similar to those of the data throughout the angular range and generally describe the shapes of the spectra quite well. The QMD (GEMINI) calculation predicts proton spectral shapes in reasonable agreement with the experimental data, but suffers from a drastic overprediction of the yield of protons as was already observed in Figs. 7 and 9.

Figure 17 shows energy spectra of α particles for the different angles in the AMPHORA detector as compared to the multifragmentation calculation, the GEMINI calculation, and the QMD calculation, respectively. The multifragmentation calculation again predicts energy spectra that are softer than those observed in the experimental data. The GEMINI calculation shows some general agreement with the data while the shapes of the α particle energy spectra predicted by the QMD (GEMINI) calculation are in somewhat better general agreement with the experimental spectra for angles forward of 45°. It should be noted that each calculation exhibits some deficiency in yield for α particles at backward angles.

The top panel in Fig. 18 compares the energy spectra of IMF's predicted by the multifragmentation model to the experimental data. The energy spectra of all products are softer than those observed in the experiment, again reflecting the low barriers resulting from the highly expanded system assumed in this model. The center panel of Fig. 18 shows the predictions of the GEMINI calculation compared to the experimental data. The shapes of the spectra show a reasonable fit to the data; however,

the yield distribution is not reproduced as was initially observed in the charge distribution of Fig. 9.

The bottom panel represents the prediction of the QMD calculation with the GEMINI afterburner. Both the shapes of the energy spectra and the yields are reproduced over the entire range of Z. The angular distribution predicted by the QMD falls off slightly faster than the experiment for heavier fragments.

VI. EVENT CHARACTERISTICS

To this point we have found that the QMD (GEMINI) calculation provides a good overall agreement with many of the experimental observables suggesting that both the dynamics and the statistical aspects of the collision and decay are being treated in a reasonable way. Given the generally good agreement of the QMD model (with the

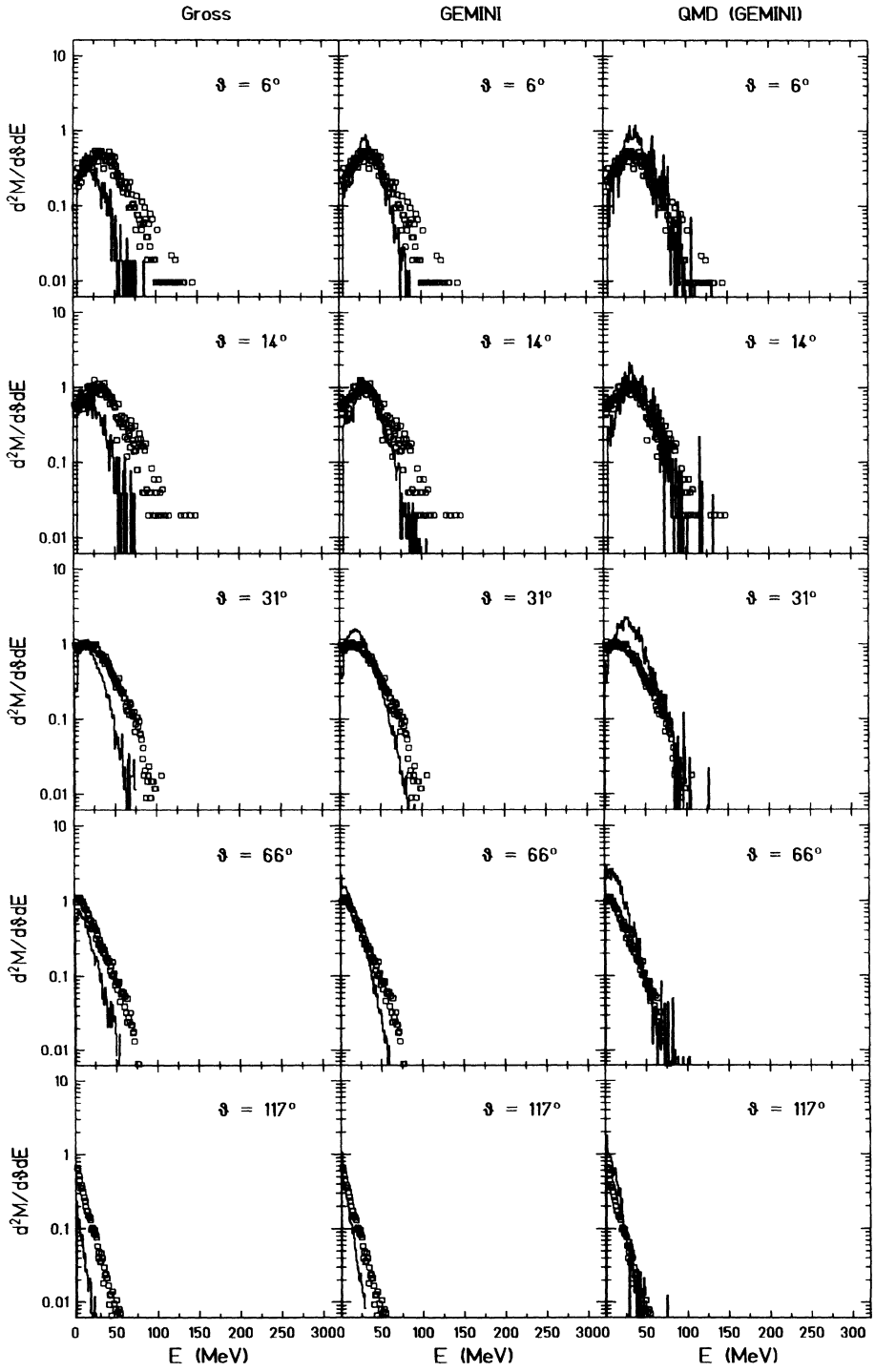

FIG. 16. Proton energy spectra of model calculations compared to experimental data for selected angles. Left, Gross multifragmentation model; center, GEMINI calculation; right, QMD with GEMINI afterburner. Open points represent the experimental data and the solid histograms represent the predictions of the model calculations.

GEMINI afterburner) it is instructive to inquire further into the types of collisions which the model predicts. This we do by first determining the impact parameter ranges in the model which lead to the regions of high and low $\ln S_2'$ in Fig. 12(d). The impact parameter distributions that lead to these small $\ln S_2'$ and large $\ln S_2'$ events are shown in Figs. 19(a) and 19(b), respectively. In the calculation the large $\ln S_2'$ events result from larger impact parameters than do the small $\ln S_2'$ events. A closer examination of event types indicates that, although there is significant mixing, in the QMD portion of the calculation, the small impact parameter events generally lead to an exited mononucleus while the higher impact parameter events often have two large primary fragments in the exit channel. Thus, in the QMD model calculation at least, the most complex events are either those

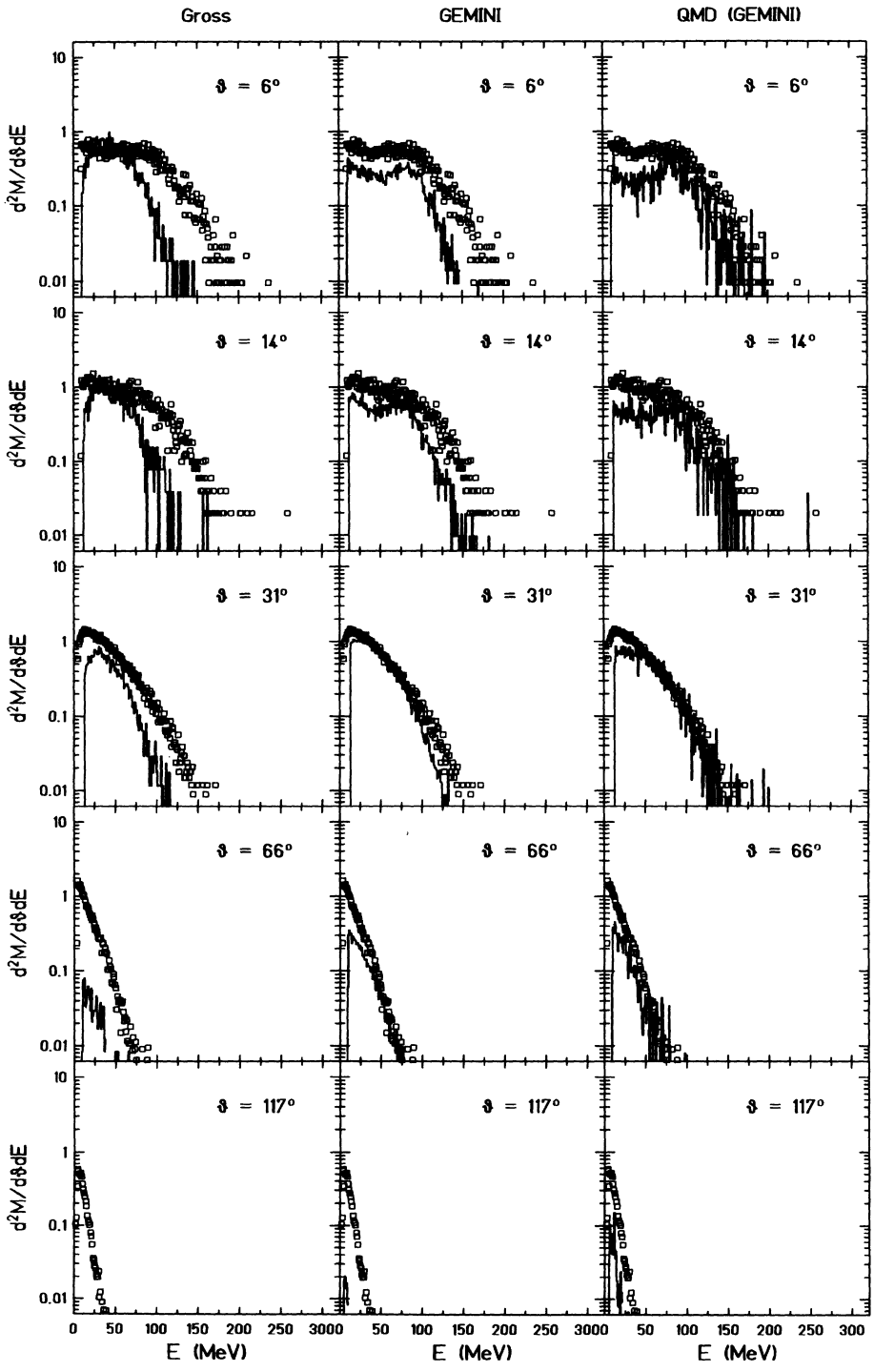

FIG. 17. α-particle energy spectra of model calculations compared to experimental data for selected angles. Left, Gross multifragmentation model; center, GEMINI calculation; right, QMD with GEMINI afterburner. Open points represent the experimental data and the solid histograms represent the predictions of the model calculations.

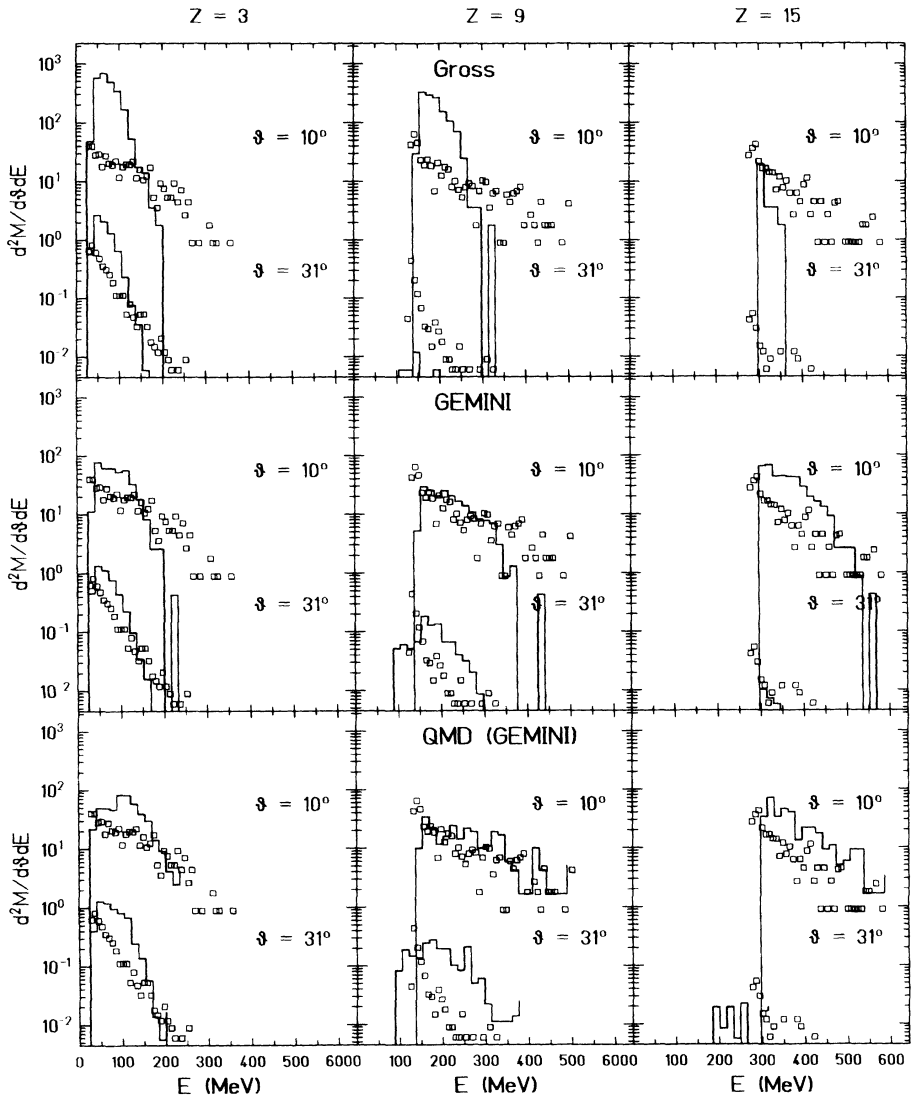

FIG. 18. IMF energy spectra of model calculations compared to experimental data for selected and selected charges. Top, Gross multifragmentation model; center, GEMINI calculation; bottom, QMD with GEMINI afterburner. Open points represent the experimental data and the solid histograms represent the predictions of the model calculations.

in which the binary nature of the collision is not forgotten even though the nucleon momentum distribution is equilibrated or those in which angular momentum plays a very important role.

This impact parameter dependence has led us to investigate the extent to which large S_2' events such as those seen in our data could simply be viewed as resulting from the normal statistical decay of two highly excited Ca-like primary fragments produced in deeply inelastic collisions. For this purpose we have carried out statistical model deexcitation calculations for nuclei having half the mass, atomic number, and excitation energy of our $A = 70$ composite system (i.e., $A = 35$, $Z = 17$, and E_x=210 MeV) and then randomly mixed two events to simulate the deexcitation of two such nuclei produced in the same event. The two primary nuclei were assumed to have a relative velocity of 2.4 cm/ns in the center of mass frame. All center of mass events were projected into the laboratory frame, one traveling forward in the center of mass and the other traveling backward in the center of mass, and filtered through the experimental ac-

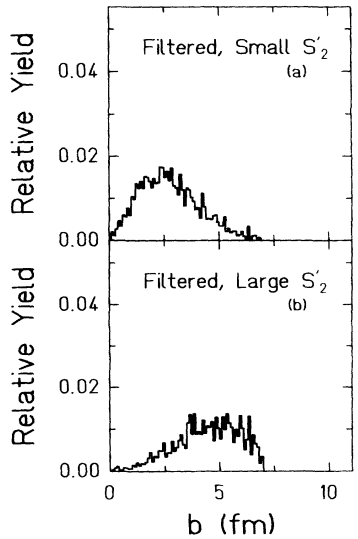

FIG. 19. The impact parameter distribution of the QMD calculation for reactions leading to (a) filtered small $\ln S_2'$ events and (b) filtered large $\ln S_2'$ events.

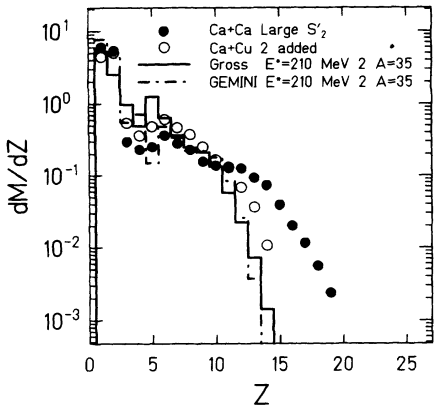

FIG. 20. The experimental yield distribution gated on large $\ln S_2'$ (solid points) compared with a multifragmentation calculation (solid line) and a GEMINI calculation (dot-dashed line) in which two mass-35 nuclei having excitation energies of 210 MeV are allowed to deexcite and then are added together and filtered through the detector acceptance and with an empirical mixing for the decay of two ^{40}Ca nuclei each with 210 MeV excitation energy (open circles).

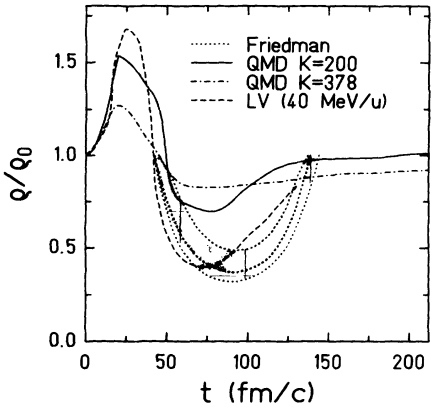

FIG. 21. Density vs time for different model calculations. The shaded area represents the ranges of expansion predicted by the EES model of Friedman for different values of assumed E_{expan}. The dotted curve showing the least expansion represents the case with E_{expan}=0 and the dotted curve showing the most expansion represents the case with E_{expan}=100 MeV. The dashed curve represents a Landau-Vlasov calculation, the solid curve represents the QMD calculation with $K = 200$, and and the dot-dashed curve represents the QMD calculation with $K = 378$.

ceptance. Calculations were done with both the GEMINI code and the Gross multifragmentation code. Not surprisingly, in each case only large S_2' events result from those simulations. The yield distributions resulting from those calculations, shown in Fig. 20, are quite similar but they exhibit significant deviations from the data.

The possibility exists that the deviations simply reflect the inadequacy of the model simulations even though the QMD model with the GEMINI afterburner has been shown to reproduce much of the experimental data for IMF production. Therefore we have used results of a study of 35 MeV/nucleon ^{40}Ca+$^{\text{nat}}$Cu [48] in which the decay of the ^{40}Ca projectile was observed at different excitation energies in peripheral and midcentral collisions to carry out a similar analysis. We used that data to simulate the effect of binary collisions in our data by choosing events having excitation energies between 200 and 250 MeV and randomly adding two events together and projecting them into the laboratory frame. Again the relative velocities of the two primary fragments were 2.4 cm/ns. Products were then filtered through the detector acceptance and analyzed in the same way as our ^{40}Ca + ^{40}Ca data. The open circles in Fig. 20 show the elemental yield distribution resulting from this simulation compared to the experimental distribution gated on large $\ln S_2'$. We still observe much more IMF production in the $Z = 6$ region which corresponds to a larger event complexity than seen in our ^{40}Ca + ^{40}Ca experiment. The simple two statistical source Ca-like assumption does not explain our large $\ln S_2'$ events very well.

VII. DENSITY AND EXPANSION EFFECTS

The QMD model employed predicts some significant compression and expansion of the composite system for the violent collisions selected in our experiments. In Fig. 21 the calculated evolution of the maximum density with time is presented. In the QMD calculation using a soft equation of state with $K = 200$, a minimum density near $0.75\rho_0$ is reached for events filtered through the detector acceptance. For a harder equation of state, with $K = 378$, the minimum value is near $0.85\rho_0$, for filtered events. For comparison to the QMD calculations we present the results of the Landau-Vlasov (LV) calculation of Ref. [15] which was made for head-on collisions with a projectile energy of 40 MeV/nucleon and $K = 200$. The QMD calculation shows less compression and less expansion than the LV calculation. At least part of the difference between the QMD and the LV calculations reflects the larger range of impact parameter in the filtered QMD simulation. At impact parameters less than 1 fm the QMD calculation for unfiltered events leads to a maximum compression near $\rho = 1.5\rho_0$. The expansion seen for these unfiltered central collisions ($b \leq 1$ fm) is, however, only about 10% more than for the filtered case. This is a result of the different prescriptions used for determining which nucleons belong to the heaviest fragment which affect the expansion phase but do not affect the compression phase.

The minimum densities reached in the EES model calculations which correspond to Fig. 15 are also shown by the shaded area in Fig. 21 for the ranges of assumed expansion energies. The EES model assumes an effective compressibility of $K = 144$ and somewhat lower values of $\rho \approx 0.35\rho_0$ are reached in the EES calculations which show the best agreement with the data.

The large value of the radius parameter of the fragmenting $A = 70$, nucleus, $R_0 = 2.08$ fm, used in the Gross multifragmentation calculation could be interpreted as implying an even lower density of $\rho = \frac{1}{6}\rho_0$ for the deexciting system. However, the radius parameter of that model is essentially determined by the assumed spherical shape of the product fragments which have a radius of

$1.18A_{\text{frag}}^{\frac{1}{3}}$. To restrict the parent nucleus radius parameter to significantly lower values than $R_0 = 2.08$ fm is equivalent to placing a restriction on the allowed fragmentations. For example, in that treatment, symmetric fission of our system is not possible for $R_0 \leq 1.87$ fm. We believe that it is more appropriate to interpret the radius parameter of the Gross calculation as characterizing the outer boundary of the shape of the complex transition state of a multifragmenting nucleus [45] rather than as an indicator of low density.

In principle detailed comparisons between the data and a good model calculation could provide information on the nuclear equation of state. Since the QMD (GEMINI) calculations are in reasonably good agreement with many of the experimental observables discussed in this paper, we have explored the sensitivity of that calculation to the assumed nuclear incompressibility by making a series of calculations with $K = 378$. While this value of K leads to significantly less expansion of the system, as seen by the solid curve in Fig. 21, the changes in the various experimental observables which we have considered are small indicating a relative insensitivity to the assumed K.

Barz *et al.* [50] have suggested that a plot of $E_\perp = E \sin^2\theta$ as a function of product mass (or atomic number) can be used to estimate the magnitude of directed radial energy resulting from expansion of a system. In view of the fact that the EES model results suggest contributions to the fragment kinetic energies of the order of 0.1–0.5 MeV/nucleon from expansion we have attempted to apply such an analysis to our data. We find, however, that our results are quite sensitive to the experimental energy thresholds, which themselves increase with increasing Z and that comparisons of the data with filtered model results are inconclusive. This may not be surprising since the EES model predicts that for the range of expansion energies considered in that calculation the bulk of the IMF emission occurs at maximum expansion when the directed radial energy is zero.

VIII. CONCLUSIONS

Complete events resulting from violent central collisions of ^{40}Ca with ^{40}Ca at 35 MeV/nucleon have been isolated and analyzed. Excitation energies near 6 MeV/nucleon appear to be reached in such collisions. Based on the comparisons between the data and the results of the various model calculations several conclusions can be drawn. For the most violent events, calculations made with normal sequential binary statistical models do not reproduce the yield distributions, event complexity, or, in detail, the energy spectra. Statistical models which incorporate expansion or allow for more complex transition states than the usual binary ones are more successful at reproducing the observed yield distributions and event complexity. With some adjustment of parameters those models might produce an even better agreement than that reported here. Such models, lacking a complete treatment of the dynamic evolution of the collision, are less successful at reproducing experimental energy spectra. The QMD model which treats the dynamic evolution of the system provides a good overall description of the experimental observables. The model predicts a proton multiplicity well above that observed and an α-particle multiplicity well below that observed. This might be improved in antisymmetrized models under development [37]. However, even when followed to a long time ($\sim$ 1000 fm/c), the model significantly underestimates the fragment yield. When a statistical model afterburner, which treats all decay channels, is used after 100 fm/c, more fragments are produced and the results are in good agreement with much of the yield distribution and event complexity observed in the experiment. This requirement of an appropriate afterburner has been noted by other authors [29,46]. A more complete inclusion of the most important quantum mechanical effects might solve the need for an afterburner and provide a complete description of the reaction [47].

The QMD model calculations suggest that, even though high excitation energy and low density is reached, the most central collisions do not usually lead to multifragment final states. In the model the multifragment events come primarily from violent collisions at larger impact parameters. Since equilibration appears to be achieved in these collisions, this suggests that angular momentum effects are important in the multifragment emission processes which we have observed. We note that this is the case even though the various "centrality" determinations employed all indicate very central events.

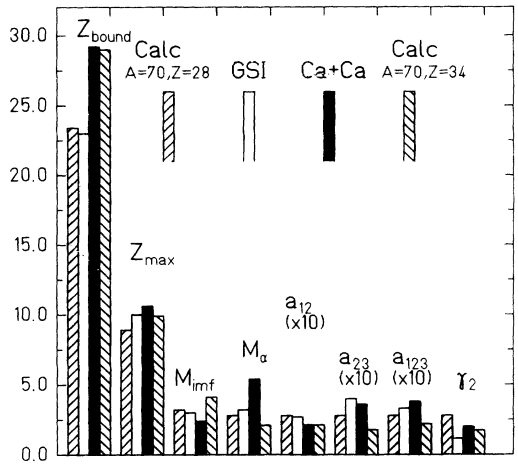

FIG. 22. Comparison of various experimental observables in ^{40}Ca + ^{40}Ca to results of 600 MeV/nucleon ^{197}Au + Cu. The Gross multifragmentation calculation is shown for both the ^{40}Ca + ^{40}Ca system and for a system with the same mass, but an N/Z ratio which corresponds to ^{197}Au. Z_{bound} is the sum of all charges in an event having $Z \geq 2$, Z_{max} is the charge of the heaviest fragment observed in an event, M_{IMF} is the average IMF multiplicity per event, M_α is the average α-particle multiplicity per event, a_{12} is the asymmetry of the heaviest fragment relative to the second heaviest fragment, a_{23} is the asymmetry of the second heaviest fragment relative to the third heaviest fragment, a_{123} is the three-body asymmetry of the three largest fragments, and $\gamma_2 = \frac{\sigma_e^2}{\langle Z \rangle_e^2} + 1$ where σ_e^2 is the variance of the charge distribution in the event and $\langle Z \rangle_e$ is the the mean charge of the event.

Similar effects must be operational in other reported multifragmentation studies.

In closing we wish to point out similarities between our data and data from the 600 MeV/nucleon ^{197}Au on various targets from an ALADIN experiment [12]. By adjusting the excitation energy input to a multifragmentation model Li and Gross [49] and Barz *et al.* [50] have reproduced the $Z_{\rm bound}$ vs $M_{\rm Imf}$ correlation and other moments of the fragment distributions seen in the ALADIN data. Li and Gross [49] estimated for central collisions of ^{197}Au with ^{63}Cu that the decaying projectilelike fragment has mass near 70 and an excitation energy per nucleon of 6 MeV, very near to the mass and excitation energy that of our system. We show in Fig. 22 comparisons of different variables for our data and the ALADIN data. We also show the results of the multifragmentation calculation of Gross for those variables both for our system and for the ALADIN data where we have assumed that the deexciting $A = 70$ nucleus has an N/Z ratio of ^{197}Au. For the two experiments we note a nearly identical pattern in the magnitudes of the different quantities considered. Our data for a system with $N = Z$ show a higher $Z_{\rm bound}$ than the ALADIN data. This is essentially accounted for by the higher α particle multiplicity. The values of $Z_{\rm max}$ and of all other variables presented in Fig. 22 are very similar for the two systems, indicating that the multifragmenting system is much the same in the two experiments. This result is surprising because of the extreme difference between the energies and colliding masses of the two systems and because of the differences in compression and expansion effects expected for the two. Significant compression and expansion is predicted for central collisions in the ^{40}Ca + ^{40}Ca system while the projectile remnants detected in the ALADIN experiment are expected to result from a relatively uncompressed, but highly excited entity which undergo large thermal expansion [51]. Energy conservation indicates that total excitation energies in our system cannot be much higher than the 6 MeV/nucleon that we have estimated. The similarity of our results to the ALADIN results for small impact parameter lends support to the arguments of Refs. [49] and [50] regarding the excitation energies at freeze-out in the ALADIN data.

ACKNOWLEDGMENTS

We thank D. H. E. Gross, W. M. Friedman, H. Horiuchi, T. Maruyama, H. Xu, K. Niita, E. Suraud, and M. Blann for many helpful discussions and for making their calculations or codes available to us. We thank the staff of the SARA Accelerator facility for their excellent support during the run. This work was supported by the U.S. Department of Energy under Grant No. DE-FG05-86ER40256, the National Science Foundation, the Robert A. Welch Foundation, and the Centre National de Recherche Scientifique.

[1] E. Bauge, A. Elmaani, Roy A. Lacey, J. Lauret, N. N. Ajitanand, D. Craig, M. Cronqvist, E. Gualtieri, S. Hannuschke, T. Li, B. Llope, T. Reposeur, A. Vander Molen, G. D. Westfall, J. S. Winfield, J. Yee, S. Yennnello, A. Nadasen, R. S. Tickle, and E. Norbeck, Phys. Rev. Lett. **70**, 3705 (1993).

[2] D. R. Bowman, G. F. Peaslee, N. Carlin, R. T. de Souza, C. K. Gelbke, W. G. Gong, Y. D. Kim, M. A. Lisa, W. G. Lynch, L. Phair, M. B. Tsang, C. Williams, N. Colonna, K. Hanold, M. A. McMahan, G. J. Wozniak, and L. G. Moretto, Phys. Rev. Lett. **70**, 3534 (1993).

[3] R. Bougault, J. Colin, F. Delaunay, A. Genoux-Libain, A. Hajfani, C. Le Brun, J. F. Lecolley, M. Louvel, and J. C. Steckmeyer, Phys. Lett. B **232**, 291 (1989).

[4] R. T. de Souza, L. Phair, D. R. Bowman, N. Carlin, C. K. Gelbke, W. G. Gong, Y. D. Kim, M. A. Lisa, W. G. Lynch, G. F. Peaslee, M. B. Tsang, H. M. Xu, and F. Zhu, Phys. Lett. B **268**, 6 (1991).

[5] D. R. Bowman, C. M. Mader, G. F. Peaslee, W. Bauer, N. Carlin, R. T. de Souza, C. K. Gelbke, W. G. Gong, Y. D. Kim, M. A. Lisa, W. G. Lynch, L. Phair, M. B. Tsang, C. Williams, N. Colonna, K. Hanold, M. A. McMahan, G. J. Wozniak, L. G. Moretto, and W. A. Friedman, Phys. Rev. C **46**, 1834 (1992).

[6] T. Li, W. Bauer, D. Craig, M. Cronqvist, E. Gualtieri, S. Hannuschke, R. Lacey, W. J. Llope, T. Reposeur, A. M. Vander Molen, G. D. Westfall, W. K. Wilson, J. S. Winfield, J. Yee, S. J. Yennello, A. Nadasen, R. S. Tickle, and E. Norbeck, Phys. Rev. Lett. **70**, 1924 (1993).

[7] M. Louvel, T. Hamdani, G. Bizard, R. Bougault, R. Brou, H. Doubre, D. Durand, Y. El Masri, H. Fugiwara, A. Genoux-Lubain, K. Hagel, A. Haifani, F. Hanappe, S. C. Jeong, G. M. Jin, S. Kato, J. L. Laville, C. Le Brun, J. F. Lecolley, S. Lee, T. Matsuse, T. Motobayashi, J. P. Patry, A. Péghaire, J. Péter, N. Prot, R. Régimbart, F. Saint-Laurent, J. C. Steckmeyer, and B. Tamain, Nucl. Phys. **A559**, 137 (1993).

[8] W. Q. Shen, J. Péter, G. Bizard, R. Brou, D. Cussol, M. Louvel, J. P. Patry, R. Régimbart, J. C. Steckmeyer, J. P. Sullivan, B. Tamain, E. Crema, H. Doubre, K. Hagel, G. M. Jin, A. Péghaire, F. Saint-Laurent, Y. Cassagnou, R. Legrain, C. Lebrun, E. Rosato, R. MacGrath, S. C. Jeong, S. M. Lee, Y. Nagashima, T. Nakagawa, M. Ogihara, J. Kasagi, and T. Motobayashi, Nucl. Phys. **A551**, 333 (1993).

[9] D. Cussol, G. Bizard, R. Brou, D. Durand, M. Louvel, J. P. Patry, J. Péter, R. Regimbart, J. C. Steckmeyer, J. P. Sullivan, B. Tamain, E. Crema, H. Doubre, K. Hagel, G. M. Gin, A. Péghaire, F. Saint-Laurent, Y. Cassagnou, R. Legrain, C. Lebrun, E. Rosato, R. MacGrath, S. C. Jeong, S. M. Lee, Y. Nagashima, T. Nakagawa, M. Ogihara, J. Kasagi, and T. Motobayashi, Nucl. Phys. **A561**, 298 (1993).

[10] L. Phair, D. R. Bowman, C. K. Gelbke, W. G. Gong, Y. D. Kim, M. A. Lisa, W. G. Lynch, G. F. Peaslee, R. T. de Souza, M. B. Tsang, and F. Zhu, Nucl. Phys. **A548**, 489 (1992).

[11] M. B. Tsang, W. C. Hsi, W. G. Lynch, D. R. Bowman, C. K. Gelbke, M. A. Lisa, G. F. Peaslee, G. J. Kunde, M. L. Begemann-Blaich, T. Hofmann, J. Hubele, J. Kempter, P. Kreutz, W. D. Kunze, V. Lindenstruth, U. Lynen, M. Mang, W. F. J. Müller, M. Neumann, B. Ocker, C. A. Ogilvie, J. Pochodzalla, F. Rosenberger, H. Sann, A. Schüttauf, V. Serfing, J. Stroth, W. Trautmann, A. Tucholski, A. Wörner, E. Zude, B. Zwielingski, S. Aiello, G. Immé, V. Pappalardo, G. Raciti, R. J. Charity, L. G.

Sobotka, I. Iorni, A. Moroni, R. Scardoni, A. Ferrero, W. Weidel, Th. Blaich, L. Stuttge, A. Cosmo, W. A. Friedman, and G. Pierlert, Phys. Rev. Lett. **71**, 1502 (1993).
[12] J. Hubele, P. Kreutz, J. C. Adloff, M. Begemann-Blaich, P. Bouissou, G. Imme, I. Iori, G. J. Kunde, S. Leray, V. Lindenstruth, Z. Liu, U. Lynen, R. J. Meijer, U. Milkau, A. Moroni, W. F. J. Müller, C. Ngô, C. A. Ogilvie, J. Pochodzalla, G. Raciti, G. Rudolf, H. Sann, A. Schüttauf, W. Weidel, L. Stuttge, W. Trautmann, and A. Tucholski, Z. Phys. A **340**, 263 (1991).
[13] D. H. E. Gross, Rep. Prog. Phys. **53**, 605 (1990).
[14] K. Sneppen and L. Vinet, Nucl. Phys. **A480**, 342 (1988).
[15] E. Suraud, in *Proceedings of the Symposium on Nuclear Dynamics and Nuclear Disassembly*, edited by J. B. Natowitz (World Scientific, Singapore, 1989), p. 464.
[16] W. Friedman, Phys. Rev. C **42**, 667 (1990).
[17] Ch. J. Pethick and D. G. Ravenhall, Nucl. Phys. **A471** 19c (1987).
[18] T. Maruyama, A. Ono, A. Ohnishi, and H. Horiuchi, Prog. Theor. Phys. **87**, 1367 (1992).
[19] M. Louvel, A. Genoux-Lubain, G. Bizard, R. Bougault, R. Brou, A. Buta, H. Doubre, D. Durand, Y. El Masri, H. Fugiwara, K. Hagel, T. Hamdani, F. Hanappe, S. C. Jeong, G. M. Gin, S. Kato, J. L. Laville, C. Le Brun, J. F. Lecolley, S. M. Lee, T. Matsuse, T. Motobayashi, A. Péghaire, J. Péter, R. Régimbart, F. Saint-Laurent, J. C. Steckmeyer, and B. Tamain, Phys. Lett. B **320**, 221 (1994).
[20] O. Lopez, M. Aboufirassi, A. Badala, B. Bilwes, R. Bougault, R. Brou, J. Colin, F. Cosmo, D. Durand, A. Genoux-Lubain, D. Horn, J. L. Laville, C. Le Brun, J. F. Lecolley, F. Lefebvres, M. Louvel, M. Mahi, C. Paulot, A. Péghaire, G. Rudolf, F. Scheibling, J. C. Steckmeyer, L. Stuttgé, B. Tamain, and S. Tomasevic, Phys. Lett. B **315**, 34 (1993).
[21] G. Bizard, R. Bougault, R. Brou, J. Colin, D. Durand, A. Genoux-Lubain, J. L. Laville, C. Le Brun, J. F. Lecolley, M. Louvel, J. Péter, J. C. Steckmeyer, B. Tamain, A. Badala, T. Motobayashi, G. Rudolf, and L. Stuttgé, Phys. Lett. B **302**, 162 (1993).
[22] R. T. de Souza, D. Fox, W. A. Friedman, L. Phair, D. R. Bowman, C. K. Gelbke, W. G. Gong, Y. D. Kim, M. A. Lisa, W. G. Lynch, G. F. Peaslee, M. B. Tsang, and F. Zhu, Phys. Lett. B **300**, 29 (1993).
[23] L. G. Moretto, Nucl. Phys. **A247**, 211 (1975).
[24] R. J. Charity, M. A. McMahan, G. J. Wozniak, R. J. McDonald, L. G. Moretto, D. G. Sarantites, L. G. Sobotka, G. Guarino, A. Pantaleo, L. Fiore, A. Gobbi, and K. D. Hildenbrand, Nucl. Phys. **A483**, 371 (1988).
[25] K. Hagel, M. Gonin, R. Wada, J. B. Natowitz, B. H. Sa, Y. Lou, M. Gui, D. Utley, G. Nebbia, D. Fabris, G. Prete, J. Ruiz, D. Drain, B. Chambon, B. Cheynis, D. Guinet, X. C. Hu, A. Demeyer, C. Pastor, A. Giorni, A. Lleres, P. Stassi, J. B. Viano, and P. Gonthier, Phys. Rev. Lett. **68**, 2141 (1992).
[26] D. Drain, A. Giorni, D. Hilscher, C. Ristori, J. Alarja, G. Barbier, R. Bertholet, R. Billerey, B. Chambon, B. Cheynis, J. Crançon, A. Dauchy, P. Désesquelles, A. Fontenille, L. Guyon, D. Heuer, A. Lléres, M. Maurel, E. Monnand, C. Morand, H. Nifenecker, C. Pastor, J. Pouxe, H. Rossner, J. Saint-Martin, F. Schussler, P. Stassi, M. Tournier and J. B. Viano, Nucl. Instrum. Methods Phys. Res. Sect. A **281**, 528 (1989).
[27] R. P. Schmitt, in *Proceedings of the International Conference on New Nuclear Physics with Advanced Techniques*, edited by F. A. Beck, S. Kossionides, and C. A. Calfas (World Scientific, Singapore, 1992), p. 182; U. Jahnke *et al.*, *Detectors in Heavy Ion Reactions*, Lecture Notes in Physics Vol. 178 (Springer, Berlin, 1983), p. 179.
[28] H. M. Xu, W. G. Lynch, P. Danielewicz, and G. F. Bertsch, Phys. Rev. Lett. **65**, 843 (1990).
[29] J. Cibor, J. Lukasik, Z. Majka, and H. M. Xu (private communication).
[30] M. Blann, Phys. Rev. C **31**, 1245 (1985).
[31] D. Durand, Nucl. Phys. **A541**, 266 (1992).
[32] J. Péter, D. Cussol, G. Bizard, R. Brou, M. Louvel, J. P. Patry, R. Regimbart, J. C. Steckmeyer, J. P. Sullivan, B. Tamain, E. Crema, H. Doubre, K. Hagel, G. M. Gin, A. Péghaire, F. Saint-Laurent, Y. Cassagnou, R. Legrain, C. Lebrun, E. Rosato, R. MacGrath, S. G. Jeong, S. M. Lee, Y. Nagashima, T. Nakagawa, M. Ogihara, J. Kasagi, and T. Motobayashi, Nucl. Phys. **A519**, 611 (1990).
[33] C. A. Ogilvie, D. A. Cebra, J. Clayton, S. Howden, J. Karn, A. Vander Molen, G. D. Westfall, W. K. Wilson, and J. S. Winfield, Phys. Rev. C **40**, 654 (1989).
[34] J. Péter, J. P. Sullivan, D. Cussol, G. Bizard, R. Brou, M. Louvel, J. P. Patry, R. Regimbardt, J. C. Steckmeyer, B. Tamain, E. Crema, H. Doubre, K. Hagel, G. M. Jin, A. Peghaire, F. Saint-Laurent, Y. Cassagnou, R. Legrain, C. Lebrun, E. Rosato, R. MacGrath, S. C. Jeong, S. M. Lee, Y. Nagashima, T. Nakagawa, M. Ogihara, J. Kasagi, and T. Motobayashi, Phys. Lett. B **237**, 187 (1990).
[35] A. Kerambrun, Ph.D. thesis, Université de Caen, Report No. LPCCT93-02, 1993.
[36] K. Niita, W. Cassing, and U. Mosel, Nucl. Phys. **A504**, 391 (1989).
[37] A. Ono, H. Horiuchi, and T. Maruyama, Report No. KUNS 1180, 1993.
[38] D. Utley, Ph.D. thesis, Texas A&M University, 1993 (unpublished).
[39] Y. Lou, Ph.D. thesis, Texas A&M University, 1994 (unpublished).
[40] J. Li (unpublished).
[41] X. Campi, J. Phys. A **19**, L917 (1986).
[42] J. Richert and P. Wagner, Nucl. Phys. **A517**, 399 (1990).
[43] G. Fai and J. Randrup, Nucl. Phys **A404**, 551 (1983).
[44] W. Friedman (private communication).
[45] G. X. Dai, J. B. Natowitz, R. Wada, Y. N. Lou, K. Hagel, and B. Xiao, Nucl. Phys. **A568**, 601 (1994).
[46] G. Peilert, J. Konopka, H. Stöcker, W. Greiner, M. Blann, and M. G. Mustafa, Phys. Rev. C **46**, 1457 (1992).
[47] J. Schnack, Ph.D. thesis, Technische Hochschule Darmstadt, 1994.
[48] A. Lleres, A. Giorni, H. Elhage, M. E. Brandan, A. J. Cole, P. Désesquelles, D. Heuer, A. Menchaca-Rocha, J. B. Viano, F. Benrachi, B. Chambon, B. Cheynis, D. Drain, and C. Pastor, Phys. Rev. C **48**, 2753 (1993).
[49] Bao-An Li and D. H. E. Gross, Phys. Lett. B **303**, 225 (1993).
[50] H. W. Barz, W. Bauer, J. P. Bondorf, A. S. Botvina, R. Donangelo, H. Schulz, and K. Sneppen, Nucl. Phys. **A561**, 466 (1993).
[51] W. Trautmann, in *Proceedings of the International Workshop XXII on Gross Properties of Nuclear Excitations, Hirschegg*, edited by Hans Feldmeier and Wolfgang Nörenberg [Gesellschaft für Schwerionenforschung (GSI), Darmstadt, 1994], p. 10.

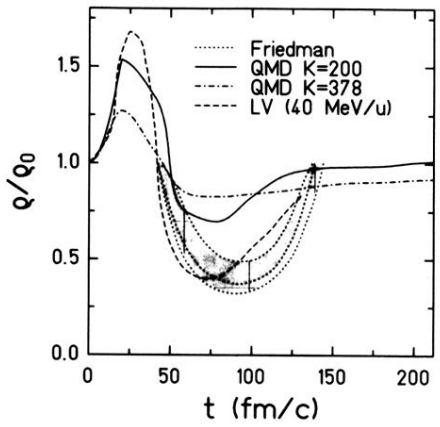

FIG. 21. Density vs time for different model calculations. The shaded area represents the ranges of expansion predicted by the EES model of Friedman for different values of assumed $E_{\mathbf{expan}}$. The dotted curve showing the least expansion represents the case with $E_{\mathbf{expan}}$=0 and the dotted curve showing the most expansion represents the case with $E_{\mathbf{expan}}$=100 MeV. The dashed curve represents a Landau-Vlasov calculation, the solid curve represents the QMD calculation with $K = 200$, and and the dot-dashed curve represents the QMD calculation with $K = 378$.